

Long Range and Short Range Magnetic Order in Orthorhombic LiMnO_2

J. E. Greedan¹ and N. P. Raju

Brockhouse Institute for Materials, McMaster University, Hamilton L8S 4M1, Canada

and

I. J. Davidson

Institute for Chemical Process and Environmental Technology, NRC, Montreal Road, Ottawa, K1A 0R6, Canada

Received June 14, 1996; in revised form October 9, 1996; accepted October 15, 1996

The magnetic properties of orthorhombic LiMnO_2 have been investigated in detail for the first time. The susceptibility data show several features including a Curie–Weiss regime from 600 to 800 K with $\theta_p = -1056(13)$ K and $\mu_{\text{eff}} = 4.82 \mu_B/\text{Mn}^{3+}$, a broad maximum at 360 K, and a field-cooled (FC), zero field cooled (ZFC) divergence below 100 K. The broad maximum indicates two-dimensional rather than one-dimensional short-range spin correlations. A Néel temperature for a transition to three-dimensional long-range order is seen at 261.5 K from both neutron diffraction and the magnetic heat capacity behavior as determined from the susceptibility data. The magnetic structure has been solved from neutron diffraction data and has a propagation vector of $k = (1/2 \ 1/2 \ 1/2)$ and an ordered magnetic moment of $3.69(4) \mu_B/\text{Mn}^{3+}$ with a preferred direction parallel to the b axis. The neutron scattering data also provide evidence for two-dimensional short-range correlations above T_c at 271 K in the form of a feature with a Warren line shape. The long- and short-range order are discussed in terms of the crystal structure which is of the ordered NaCl type distorted by the presence of the Jahn–Teller ion, Mn^{3+} . © 1997 Academic Press

1. INTRODUCTION

Orthorhombic LiMnO_2 has been known since 1956 and is one of a number of so-called ordered-NaCl structures (1). The detailed crystal structure was deduced first from powder and later from single crystal X-ray diffraction data and is described in $Pmmn$ (2). This compound has received attention recently as a precursor for a cathode material in solid state lithium batteries, as it transforms to a defect spinel structure upon electrochemical removal of Li (3–5). In spite of this increased level of activity there have been no studies of basic physical properties such as magnetism.

¹ To whom correspondence should be addressed.

Certain features of the crystal structure suggest that this material may have interesting magnetic properties. First, the local environment of the Mn–O octahedron is distorted significantly due to the presence of the Jahn–Teller ion Mn^{3+} , $3d^4$. There are two long axial Mn–O bonds of $2.298(1)$ Å directed along the b axis and two nearly equal equatorial pairs at $1.920(9)$ and $1.937(9)$ Å. In typical ordered rock salt phases such as LiNiO_2 one finds layers of nearly regular edge-sharing octahedra which stack in a direction normal to the close-packed oxygen layers, resulting in rhombohedral symmetry. For LiMnO_2 the oxygen sublattice is sufficiently distorted that the Mn–O and Li–O layers form a zigzag pattern with a stacking direction nearly 45° to that for the typical case (3).

As a result of all of the above, the Mn sublattice has some unusual features as illustrated in Fig. 1. First, the hexagonal symmetry found in the rhombohedral, ordered NaCl phases is still present but the layers are distorted significantly and folded, the fold angle being 111° . The basic edge-sharing triangular motif is preserved but the triangles are distorted to isosceles with one edge at the a -axis distance of 2.806 Å and the other two at 3.09 Å with angles of 63° , 63° , and 54° . Alternatively, one can also view the sublattice as comprised of linear chains of Mn atoms parallel to the a axis with a short Mn–Mn separation of 2.806 Å. Two chains run through each cell at $z = 0.633$ and 0.367 with an interchain Mn–Mn separation of 3.09 Å.

The configuration of the Mn–O octahedra is shown in Fig. 2. As the octahedra share edges, the intra- and inter-chain Mn–O–Mn angles, relevant for superexchange, are essentially identical at $93.3(2)^\circ$ and $92.8(4)^\circ$, respectively. The zigzag Mn–O layers are connected via intervening Li–O layers with a closest interlayer Mn–Mn distance of 5.00 Å.

Figure 2 is also useful as an aid to understanding the orbital symmetry considerations which determine the

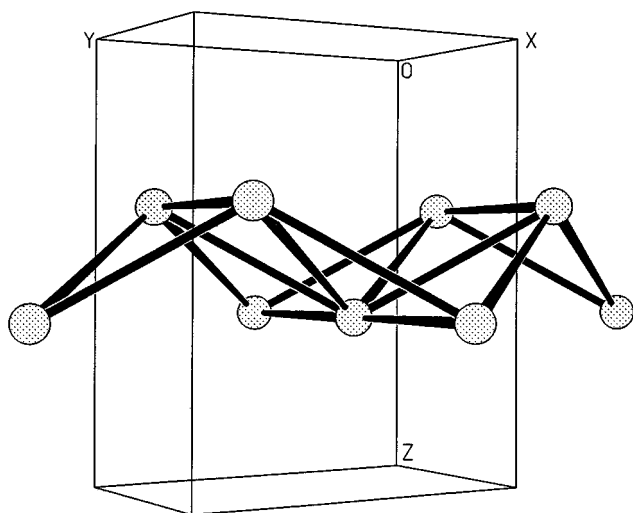


FIG. 1. The Mn sublattice in LiMnO_2 .

magnetic exchange pathways in this material. As a tetragonal elongation is involved, the Mn^{+3} configuration will be $t_{2g}^3 d_z^1 d_{x^2-y^2}^0$. The intrachain Mn–O–Mn 90° interaction will involve the empty $d_{x^2-y^2}$ orbitals so this may be weak. The intrachain Mn–Mn interaction will occur via the half-filled $t_{2g}(d_{xz})$ orbitals and will be strongly antiferromagnetic. The interchain exchange coupling is also by a 90° Mn–O–Mn pathway but the orbitals involved are d_{z^2} –O– $d_{x^2-y^2}$ and this will be relatively weaker and probably antiferromagnetic as discussed by Goodenough in comparison with other Mn^{3+} materials showing a static Jahn–Teller distortion (6). Thus, it is a good assumption that the strongest exchange interaction in this material will be the antiferromagnetic Mn–Mn interaction along the short a axis.

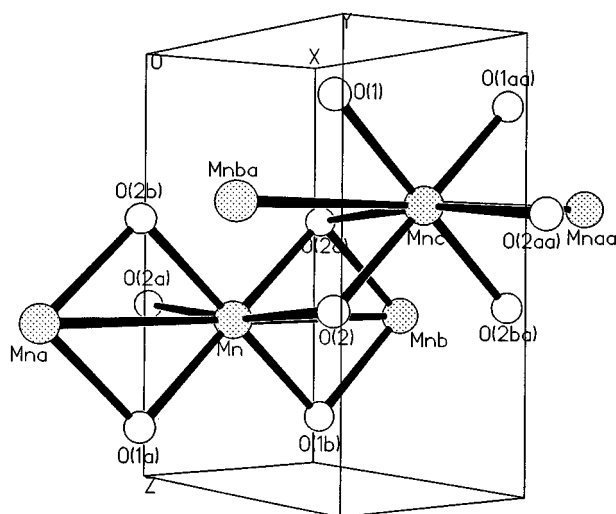


FIG. 2. Edge-sharing Mn–O octahedra in LiMnO_2 .

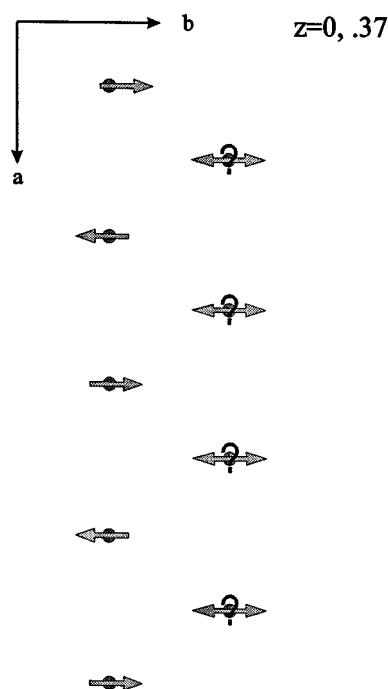


FIG. 3. Possible symmetry cancellation effect between antiferromagnetically correlated Mn chains in LiMnO_2 .

In addition, geometric effects may also be important. As already argued, the Mn sublattice can be regarded as a set of interwoven a -axis chains with atom positions in adjacent chains displaced along c and also along a by $(1/2\ 0\ 0)$ such that an atom in one chain centers two spins in each adjacent chain, as depicted in Fig. 3. If the intrachain interactions are strongly antiferromagnetic as expected, the interchain coupling may be subject to a symmetry cancellation as shown. Thus, at the highest temperatures the magnetic correlations would be one dimensional with cross-overs to two and, ultimately, three dimensionality as the temperature is lowered.

2. EXPERIMENTAL

(a) Sample Preparation LiMnO_2

Samples of the orthorhombic form of LiMnO_2 were prepared from Fisher Scientific Certified MnO_2 and Aldrich 99.997% pure Li_2CO_3 . The powdered reagents were intimately mixed by grinding and pelletizing. Then the pellets were loaded into high purity alumina crucibles and fired in a horizontal tube furnace under a flow of argon gas. The mixture was first calcined at 600 – 650°C for several hours to remove the CO_2 , and then baked at 800 – 1000°C for 1 to 3 days. Generally, one or two more grindings and firings were required to achieve a well crystallized product.

(b) Magnetic Measurements

Magnetic susceptibility data were obtained using a Quantum Design SQUID magnetometer in the temperature range from 5 to 800 K using a 10^{-2} T applied field.

(c) Neutron Diffraction

Powder neutron diffraction data were collected at the McMaster Nuclear Reactor using a neutron wavelength of 1.392 Å and a position sensitive detector which has been described previously (7). A thin-walled vanadium can was used for room temperature experiments and at low temperatures an aluminum sample holder containing helium exchange gas and sealed with an indium gasket was utilized. The sample was cooled by a closed-cycle refrigerator in the temperature range from 10 to 271 K. Data analysis was carried out using either DBWS PC9600 or FULLPROF (8,9).

3. RESULTS AND DISCUSSION

(a) Magnetic Susceptibility

Figure 4 displays susceptibility data for LiMnO_2 over the range from 5 to 800 K. The most striking features are the maximum below 50 K, the field-cooled (FC), zero field cooled (ZFC) divergence below 100 K, and the broad maximum (inset) centered at about 360 K. The occurrence of the broad maximum is evidence for the presence of short-range magnetic correlations, consistent with speculations presented previously. In principle the dimensionality of the correlations can be assessed by fitting the data to models for

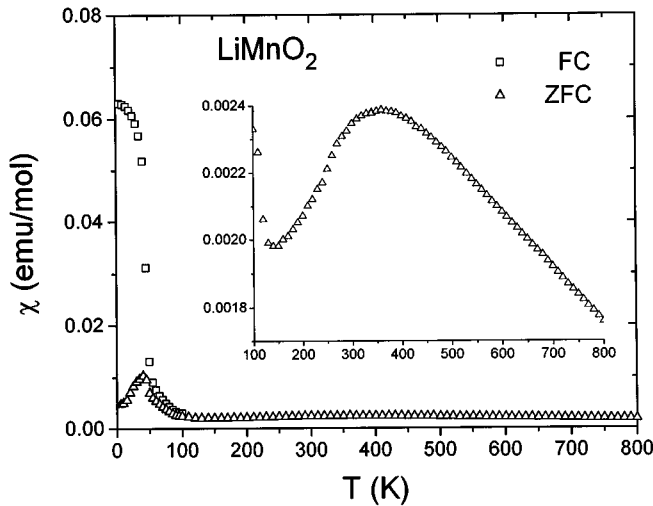


FIG. 4. Magnetic susceptibility data for LiMnO_2 from 5 to 800 K at an applied field of 10^{-2} T. The squares and triangles represent zero field cooled and field cooled conditions, respectively. The inset shows the broad, weak maximum at about 360 K.

one- and two-dimensional magnetic lattices. An attempt to fit to a one-dimensional model, $S = 2$, failed, thus indicating that the dominant correlations in this temperature regime are two-dimensional. This conclusion will be reinforced by the neutron scattering results in the following section. Unfortunately, there exist no calculations for the two dimensional magnetic lattice pertinent here, a puckered, distorted hexagonal net, so it is impossible to carry out a detailed fitting to extract the exchange constant. In any case there is no clear evidence for purely one-dimensional correlations in the temperature regime investigated which indicates that the intrachain and interchain exchange interactions must be comparable.

In Fig. 5 the inverse susceptibility is plotted which shows an approach to the Curie-Weiss law at the highest temperatures. The extracted constants are $C = 2.90(2)$ emu K mol $^{-1}$ from which $\mu_{\text{eff}} = 4.82 \mu_B/\text{Mn}^{3+}$ can be derived compared to $4.90 \mu_B$ for a $S = 2$ free ion. A very large, negative $\theta_p = -1056(13)$ K is found which indicates the presence of strong antiferromagnetic interactions. The data also show a subtle inflection point near 250 K. The inset displays a plot of $d(\chi T)/dT$ in this temperature range. This function has been shown to be a measure of the magnetic contribution to the heat capacity (10) and the pronounced maximum at 260 K indicates the presence of a magnetic phase transition.

(b) Neutron Diffraction

A room temperature diffraction pattern was obtained and the data were refined by the Rietveld method primarily as a check on the sample purity and to compare with the

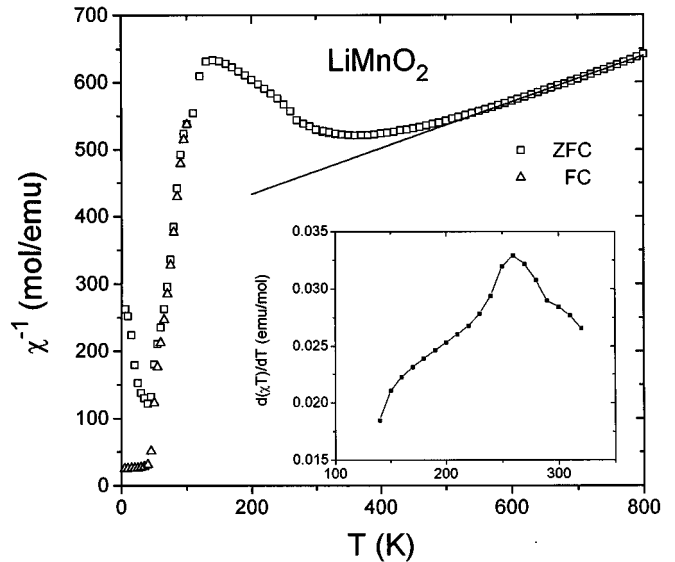


FIG. 5. The inverse magnetic susceptibility of LiMnO_2 . The inset shows the Fisher heat capacity (10) identifying a transition at 261 K.

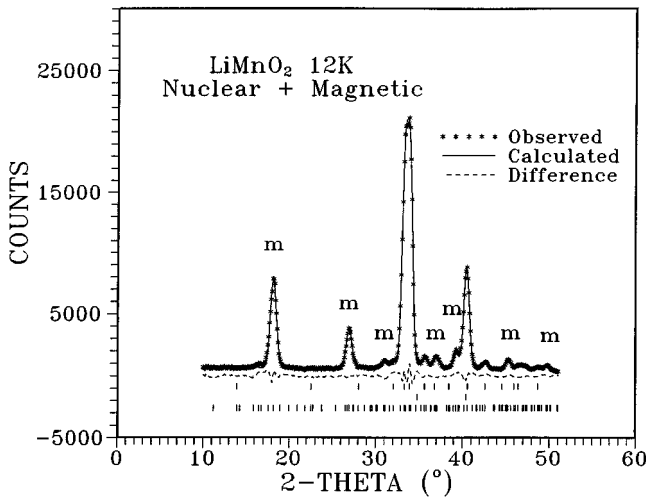


FIG. 6. Low angle part of the neutron diffraction powder pattern for LiMnO_2 at 11 K. Reflections of magnetic origin are marked with an m. The solid line is a three-component Rietveld fit including the chemical structure, the Al sample can, and the magnetic structure of Fig. 7. The vertical tick marks locate the Bragg peak positions for the three respective components, the chemical structure, the sample can, and the magnetic structure (top to bottom).

previous X-ray diffraction results. Neutron diffraction is often a more rigorous test of sample purity than X-ray diffraction as the neutron beam probes the entire sample volume. No additional phases were detected and the refined unit cell parameters and atomic positions agreed very well with the results reported previously [2].

Upon cooling from room temperature to 11 K several strong reflections appeared, as shown in Fig. 6, which could be indexed on a unit cell $2a \times 2b \times 2c$ with respect to the chemical cell which implies a magnetic propagation vector, $k = (1/2 \ 1/2 \ 1/2)$. A model for the magnetic structure at 11 K was found readily by assuming antiferromagnetic order within each a -axis chain, that the chains in each puckered layer couple antiferromagnetically, and that the interplanar coupling is also antiferromagnetic. The best agreement was found for a collinear spin model with an ordered moment of $3.69(4) \mu_B$ with a preferred spin direction parallel to the b axis as depicted in Fig. 7. The fit in Fig. 6 is to a three-component model which includes the chemical structure, the aluminum sample can, and the magnetic structure of Fig. 7. The relevant refinement details are listed in Table 1.

The temperature dependencies of the two most intense magnetic reflections, $(1/2 \ 1/2 \ 1/2)$ and $(1/2 \ 1/2 \ 3/2)$, are shown in Fig. 8. First, note the clear indication of a critical or Néel temperature, $T_c = 260$ K, confirming the susceptibility and magnetic heat capacity results of Figs. 4 and 5. A more precise value of T_c can be obtained by fitting data near the ordering temperature to a power law of the type $M = M_0[(T_c - T)/T_c]^\beta$, where M is the sublattice magnet-

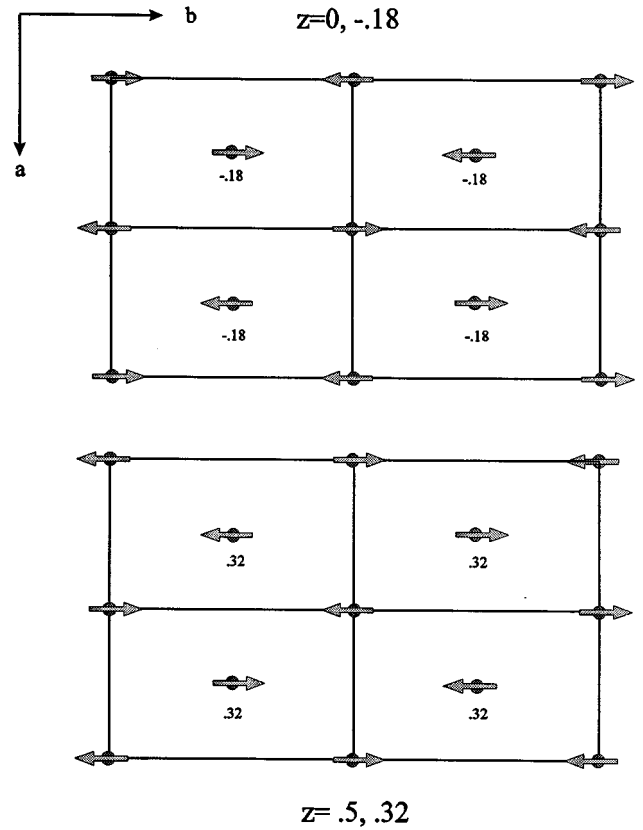


FIG. 7. A (001) projection of the magnetic structure found for LiMnO_2 .

ization, T_c is the critical temperature, and β is the critical exponent (11). The results of such a fitting are shown in Fig. 9 and the fitted parameters are $T_c = 261.5(5)$ K and $\beta = 0.376(17)$. This later value is consistent with a three-dimensional Heisenberg model which is reasonable for Mn^{3+} (11).

Also seen in Fig. 8 is the presence of an anomaly in the temperature dependence of the magnetic moment which sets in below 100 K, the temperature below which FC-ZFC irreversibilities are observed in the bulk susceptibility. Below 100 K the intensities of the strongest magnetic reflections, $(1/2 \ 1/2 \ 1/2)$ at $2\theta = 18.16^\circ$ and $(1/2 \ 1/2 \ 3/2)$ at 26.94° , deviate in a positive and a negative sense, respectively, from the Brillouin function like dependence which pertains at higher temperatures. This is due, most likely, to the onset of a small sublattice canting below 100 K. Thus, at low temperatures LiMnO_2 is a weak ferromagnet. It was not possible to determine the canting angle from the available neutron data but it is likely to be small.

One further issue concerns the characterization of the short-range magnetic order above T_c . The powder pattern at 271 K, 10 K above T_c (Fig. 10), shows that all of the magnetic Bragg peaks have disappeared but a pronounced,

TABLE 1
Refinement Details for the Magnetic Structure of LiMnO₂ at 12 K

Chemical cell	
<i>a</i>	2.806(1) Å
<i>b</i>	4.550(2) Å
<i>c</i>	5.747(2) Å
Magnetic cell	
<i>a</i>	5.612(2) Å
<i>b</i>	9.100(4) Å
<i>c</i>	11.494(4) Å
Atomic positions (<i>Pmmn</i>) ^a	
Li (2 <i>a</i>)	<i>z</i> = 0.125
Mn (2 <i>a</i>)	<i>z</i> = 0.643
O1 (2 <i>b</i>)	<i>z</i> = 0.136
O2 (2 <i>b</i>)	<i>z</i> = 0.600
Magnetic moment of Mn ³⁺	
Moment direction	[0 1 0]
Overall thermal factor, <i>B</i> ^a	0.500 (Å ²)
Agreement indices	
Overall	<i>R</i> _{wp} = 0.077
	<i>R</i> _{exp} = 0.023
Chemical structure	<i>R</i> _B = 0.016
Al sample holder	<i>R</i> _B = 0.005
Magnetic structure	<i>R</i> _B = 0.086

^a Fixed at these values, refinement had no effect on the magnetic moment value.

$$R_{wp} = \{[\sum w(Y_{OBS} - Y_{CAL}/c)^2] / \sum wY_{OBS}^2\}^{1/2},$$

$$R_{exp} = [(N - P) / \sum Y_{OBS}^2]^{1/2},$$

$$R_B = \frac{\sum (I_{OBS} - I_{CAL})}{\sum I_{OBS}}.$$

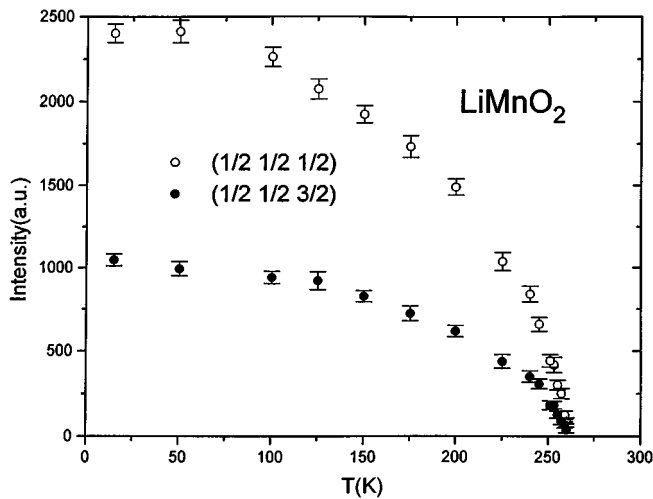


FIG. 8. Temperature dependence of the (1/2 1/2 1/2) and (1/2 1/2 3/2) magnetic Bragg peaks for LiMnO₂.

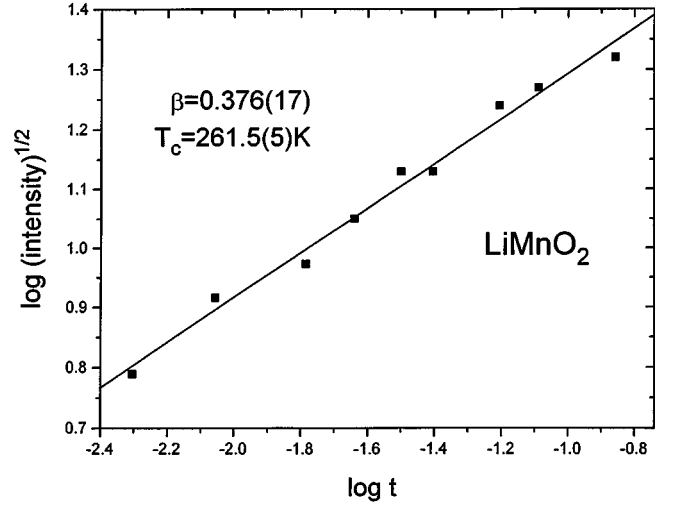


FIG. 9. A power law fit to determine *T_c* and the critical exponent β for LiMnO₂.

broad feature remains, centered at about $2\theta = 16^\circ$, which has a distinctly asymmetric shape with a relatively sharp rise at low angles followed by a more gradual decrease over several degrees to higher angles. This peak shape is of the Warren type which is a signal of two-dimensional correlations (12). The insert in Fig. 10 shows a fit of this peak to the Warren function. A two-dimensional correlation length of 36(1) Å can be derived using methods described previously (13). Thus, it appears that at 271 K the Mn spins are correlated within the puckered, distorted hexagonal layers which confirms the interpretation of the susceptibility data given previously.

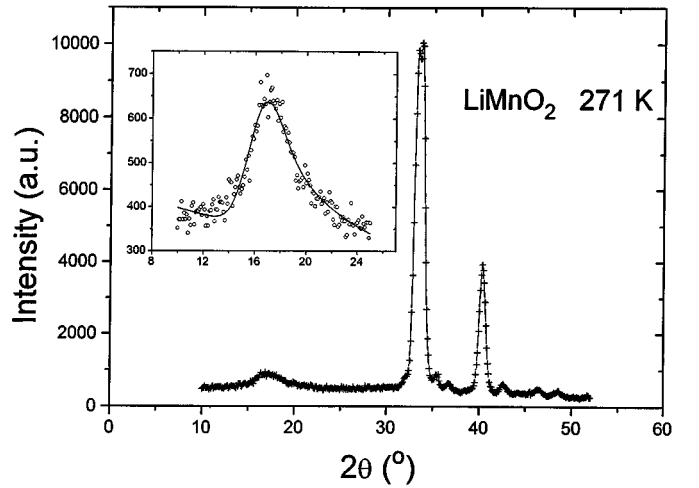


FIG. 10. Low angle neutron diffraction pattern of LiMnO₂ at 271 K showing the broad, asymmetric Warren-type reflection at about 16° which represents magnetic short-range order. The inset shows a fit of this peak to the Warren function.

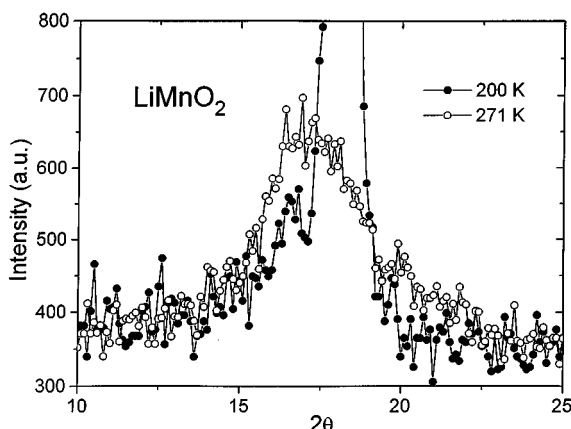


FIG. 11. Comparison of neutron scattering at 271 and 200 K at the positions of the Warren peak and the $(1/2 \ 1/2 \ 1/2)$ magnetic Bragg peak.

Finally, Fig. 11 shows that the two-dimensional correlations persist into the ordered regime and that in fact the long-range order grows at the expense of the two-dimensional order. In this figure, data at 200 K, well below T_c , and 271 K are compared after adjusting the background of the two data sets. It is clearly seen that the Warren maximum lies to slightly lower angles than the $(1/2 \ 1/2 \ 1/2)$ Bragg peak and that a vestige of the Warren feature is present at 200 K but with a much diminished amplitude.

4. SUMMARY

Although a relatively simple material, LiMnO_2 exhibits complex magnetic behavior. Crystallographic distortions due to the presence of the Jahn–Teller ion, Mn^{3+} , result in a Mn sublattice which consists of folded, distorted hexagonal layers. This results in short-range magnetic correlations which are manifested in a broad susceptibility maximum at 350 K. Evidence from both susceptibility and neutron scattering data characterize the short-range order as two dimensional. Below 261 K, long-range antiferromag-

netic order is established with a magnetic structure having a propagation vector $k = (1/2 \ 1/2 \ 1/2)$. The details of the magnetic structure are consistent with expectations that the strongest exchange constraints are antiferromagnetic within the a -axis chains and that the structure evolves by interchain coupling to form layers and finally, interlayer coupling. The ordered moment is $3.65(2) \mu_B/\text{Mn}^{3+}$ and the preferred direction is along the b axis. Evidence for the onset of spin-canting below 100 K is found from susceptibility and neutron diffraction data.

ACKNOWLEDGMENTS

We thank the Natural Science and Engineering Research Council of Canada for financial support and McMaster University for direct support of the McMaster Nuclear Reactor. C. V. Stager has provided access to the SQUID magnetometer.

REFERENCES

1. W. D. Johnston and R. R. Heikes, *J. Am. Chem. Soc.* **78**, 3255 (1956).
2. G. Dittrich and R. Hoppe, *Z. Anorg. Allg. Chem.* **368**, 262 (1969); R. Hoppe, G. Brachtel, and M. Jansen, *Z. Anorg. Allg. Chem.* **417**, 1 (1975).
3. R. J. Gummow, D. C. Liles, and M. M. Thackeray, *Mater. Res. Bull.* **28**, 1249 (1993).
4. T. Ohsuku, A. Ueda, and T. Hirai, *Chem. Express* **7**, 193 (1992).
5. I. J. Davidson, R. S. McMillan, J. J. Murray, and J. E. Greedan, *J. Power Sources* **54**, 232 (1995).
6. J. B. Goodenough, "Magnetism and the Chemical Bond." Interscience, New York, 1963.
7. J. N. Reimers, J. E. Greedan, and M. Sato, *J. Solid State Chem.* **72**, 390 (1988).
8. D. B. Wiles and R. A. Young, *J. Appl. Crystallogr.* **14**, 149 (1981).
9. J. Rodriguez-Carvajal, "FULLPROF: A Program for Rietveld Refinement and Pattern Matching Analysis" Abstracts of the Satellite Meeting on Powder Diffraction of the XV Congress of the I.U.C. p. 27 Toulouse, France, 1990.
10. M. E. Fisher, *Philos. Mag.* **17**, 1731 (1962).
11. M. F. Collins, "Magnetic Critical Scattering," pp. 12–15. Oxford Univ. Press, London, 1989.
12. B. E. Warren, *Phys. Rev.* **59**, 693 (1941).
13. J. E. Greedan, M. Bieringer, J. F. Britten, D. M. Giaquinta, and H.-C. zur Loye, *J. Solid State Chem.* **116**, 118 (1995).